Random matrix ensembles in hyperchaotic classical dissipative dynamic systems

J Odavić[1,*] and P Mali[2]

[1] Ruđer Bošković Institute, Bijenička cesta 54, 10000 Zagreb, Croatia
[2] Department of Physics, Faculty of Science, University of Novi Sad, Trg Dositeja Obradovića 4, 21000 Novi Sad, Serbia
E-mail: jodavic@irb.hr

Abstract. We study the statistical fluctuations of Lyapunov exponents in the discrete version of the non-integrable perturbed sine-Gordon equation, the dissipative AC- and DC-driven Frenkel–Kontorova model. Our analysis shows that the fluctuations of the exponent spacings in the strictly overdamped limit, which is nonchaotic, conform to an *uncorrelated* Poisson distribution. By studying the spatiotemporal dynamics, we relate the emergence of the Poissonian statistics to Middleton's no-passing rule. Next, by scanning values of the DC drive and the particle mass, we identify several parameter regions for which this one-dimensional model exhibits hyperchaotic behavior. Furthermore, in the hyperchaotic regime where roughly fifty percent of the exponents are positive, the fluctuations exhibit features of the *correlated* universal statistics of the Gaussian orthogonal ensemble (GOE). Due to the dissipative nature of the dynamics, we find that the match between the Lyapunov spectrum statistics and the universal statistics of GOE is not complete. Finally, we present evidence supporting the existence of the Tracy–Widom distribution in the fluctuation statistics of the largest Lyapunov exponent.

Keywords: dissipative systems, nonlinear dynamics, random matrix theory and extensions

*Author to whom any correspondence should be addressed.

Contents

1. Introduction

Matrices with random entries have interested physicists for a long time. The simple reason for this is that many complex and strongly-correlated many-body problems, which can be formulated in terms of ensembles of such random matrices, are found to be analytically tractable due to the underlying symmetries that these matrices entail [1]. Starting with the work of Wigner [2], ensembles of such 'integrable' Hamiltonians have been shown to naturally emerge in fields such as nuclear physics, disordered systems, string theory, transport phenomena and many others [3–5].

Random matrix theory (RMT) is a scientific discipline that involves the study of the particular universal features displayed by an ensemble of random matrices when the size of the matrix $N \to \infty$. When the matrix entries are independently and identically distributed (i.i.d.) random variables and the matrices are rotationally invariant, three universality classes or ensembles of *correlated* random matrices exist and are designated as Gaussian ensembles. Matrices with $[N \times N]$ real symmetric random entries are known as Gaussian orthogonal ensembles (GOEs), $[N \times N]$ complex Hermitian matrices are known as Gaussian unitary ensembles (GUEs), and $[2N \times 2N]$ self-dual Hermitian matrices are known as Gaussian symplectic ensembles (GSEs). In the process of diagonalization of the matrices just mentioned, the eigenvalues become correlated and each eigenvalue 'feels' the presence of the neighboring eigenvalues, leading to the phenomenon of level repulsion [6]. In the asymptotic $N \to \infty$ limit the eigenvalue distributions of such

ensembles conform to the famous semi-circle law, while the eigenvalue spacing distribution follows Wigner's universal surmise [1, 7]. An interesting variation to the standard Gaussian ensembles includes the $[N \times N]$ Wishart matrix $W = X^{\mathrm{T}}X$, where X is a rectangular $[N' \times N]$ matrix with i.i.d. entries, resulting in the Marchenko–Pastur law [8]. In the case where the eigenvalues are themselves i.i.d. random values (i.e. *uncorrelated*) with finite variance, their distribution due to the central limit theorem follows a normal (Gaussian) distribution. In this case, the eigenvalue spacings follow a Poisson distribution. To generate such an eigenvalue distribution, it is sufficient to diagonalize matrices with i.i.d. values sampled from the Gaussian distribution only along the main diagonal, e.g. see [9].

Recently, the presence of universal statistics of random matrix ensembles in the Lyapunov exponent spectrum has been demonstrated in the classical limit of the matrix model of D0-branes [10, 11] with conservative dynamics. The Lyapunov exponents measure the average exponential rate of the divergence of neighboring orbits in phase space. They are considered an indispensable tool for detecting the presence of chaos in dynamic systems [12]. The Lyapunov exponent distribution in the above mentioned supersymmetric model, used by the string theory community, was shown to follow the semi-circle law. Furthermore, in the Kuramoto model of N oscillators with a variable coupling matrix, similar findings have been reported, where the presence of a Poisson or Wigner surmise distribution in the Lyapunov exponent spacings is taken to be an indicator of synchronization behavior [13]. Historically, the authors of [14] were the first to show the existence of neighboring Lyapunov exponent repulsion, hinting at the similarities between the behavior of Lyapunov exponents and Gaussian RMT ensembles.

Motivated by the abovementioned findings, we proceed to show the existence of correlated random matrix ensemble features in a typical condensed-matter model, the classical nonlinear and hyperchaotic dynamic system with *dissipative* dynamics, the AC- and DC-driven Frenkel–Kontorova (FK) model. Moreover, within the same model, and for a particular choice of parameters when the system is nonchaotic, we show the presence of Poissonian statistics in the Lyapunov exponent spacings. We choose to work with this model because of its clear physical interpretation and enormous applicability to various existing physical systems [15]. This model represents an appropriate theoretical framework for the description of charge- and spin-density wave transport, irradiated Josephson-junction arrays, and driven colloids [16–18], Later in this paper, we show that the model considered in the regime where its Lyapunov exponents exhibit repulsion is equivalent to a realistic one-dimensional parallel array of Josephson junctions (JJs) with a stripline geometry [19].

The Lyapunov exponents are typically defined as the singular value decomposition values of the Jacobians of the linearized dynamics. The Jacobian that governs the behavior of the perturbed trajectories at the end of the time evolution of a dynamic system is composed of the product of such Jacobians at previous time steps [20, 21]. From this point of view, the eigenvalue statistics of the product of random matrices and Lyapunov exponent statistics are closely related; see [22] and references therein. Making use of this connection, a computation of the complete Lyapunov exponent spectrum has been approximately performed for the Fermi–Pasta–Ulam chain of oscillators [23]. Our work, on the other hand, is focused on identifying different dynamic regimes in the spatially

extended dissipative and AC- and DC- driven FK model from the Lyapunov spectrum. In this endeavor, we compare the Lyapunov exponents' fluctuations to the predictions of RMT.

This paper is organized in the following way. In section 2.1, we present the model and discuss the interesting regimes and model-specific nomenclature used in the paper. Next, in section 2.2, we discuss how the Lyapunov exponent spectrum is defined and its particular importance. In section 3, we present the results of our study using techniques from both RMT and the nonlinear dynamics community. We conclude in section 4.

2. Model and method

2.1. The model

The standard Frenkel–Kontorova (FK) model represents a chain of harmonically interacting identical particles with positions $\{u_i\}$ subjected to a sinusoidal substrate potential with amplitude K

$$V(u) = \frac{K}{4\pi^2}\left[1 - \cos(2\pi u)\right], \tag{1}$$

and it is defined by the Hamiltonian

$$H = \sum_i \left(\frac{m}{2}\dot{u}_i^2 + \frac{1}{2}(u_{i+1} - u_i - a_0)^2 + V(u_i)\right), \tag{2}$$

where m represents the mass of the point-like particles each indexed by the subscript i, while a_0 is the equilibrium distance of the inter-particle potential. After suitable renormalization of the model parameters and by neglecting the discreteness effects, the standard FK model reduces to the well-studied integrable sine-Gordon (sG) equation [15]. sG is applicable in a wide range of physical systems from JJs to gravity and high-energy physics [15, 24]. Systems that are described by the sG equation are known to support excitations such as topological solitons (kinks) and dynamic solitons (breathers) and attract a lot of attention from physicists despite/for being integrable. The sG equation can be extended in different ways. For instance, a common and useful extension is the perturbed sG equation. Depending on the physical system and interpretation, the perturbation is typically a damping term that breaks the integrability. A particular version of the perturbed sG equation that includes both damping and a driving term has been successful in describing long JJs [25].

In our work, we focus on the dissipatively driven FK model, i.e. a discretized version of the perturbed sG equation, which is also non-integrable and exhibits more complex dynamics compared to the sG equation and the standard FK model. Such a model is used to describe phenomena in many different physical systems [15, 26–29]. The equations of motion of the dissipatively driven FK model of N identical particles have the following form

$$m\ddot{u}_i = u_{i+1} + u_{i-1} - 2u_i - \frac{\partial V}{\partial u_i} - \dot{u}_i + F(t), \tag{3}$$
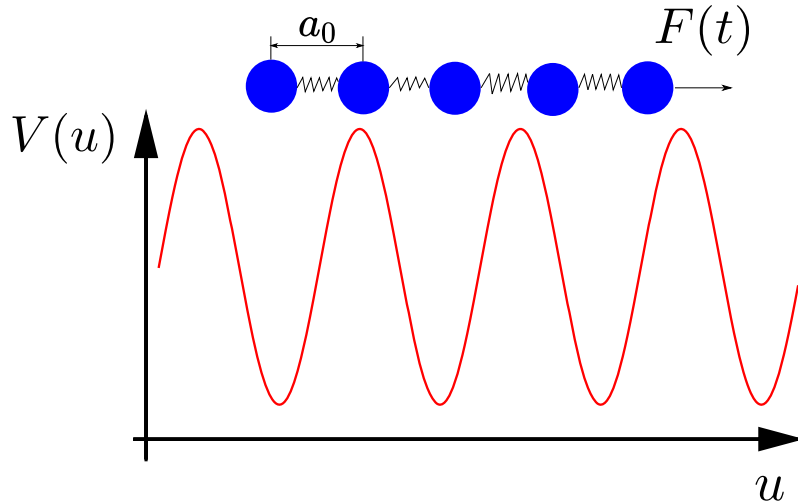
Figure 1. Sketch of the AC- and DC-driven Frenkel–Kontorova model defined by equation (2) and the equations of motion given in equation (3). The harmonically interacting particles are featureless point-like masses.

where $\dot{u}_i$ defines the dissipative term, i labels particles $i = 1, \ldots, N$, and $F(t)$ is the driving force chosen in the form $F(t) = F_{\rm dc} + F_{\rm ac}\cos(2\pi\nu_0 t)$ (see figure 1). We impose cyclic boundary conditions using $u_0 = \mod(u_N, N\omega)$, where ω represents the interparticle average distance, i.e. the average number of particles per substrate potential well [27, 30]. In literature, different regimes have been identified to exist in this model, such as the $m \to 0$ limit of equation (3) which defines the strictly overdamped limit [31], the overdamped regime for which $0 < m \leqslant \frac{1}{4(2+K)}$, and the underdamped regime otherwise [32]. To integrate the system of equation (3), we use the standard techniques described in [33] with a time step of ν_0^{-1} and a relative tolerance of 10^{-6}.

Due to the exertion of the force term $F(t)$, the dissipative FK model undergoes a dynamic phase transition from a pinned regime to the sliding particle motion regime [30, 34]. The study of critical force dynamics is an active field of research related to the description of different interesting phenomena in tribology, the traffic flow of cars on a road, and many others [15]. In our work, we primarily investigate the physics of the sliding regime where the system's response is strongly nonlinear and the dynamics is richer.

In the underdamped regime, the dissipatively driven FK model exhibits sensitivity to the initial conditions [35], i.e. chaotic dynamics, whereas in the strictly overdamped limit, the system is nonchaotic [17, 30]. In the following section, we describe how the presence of chaos is quantified using Lyapunov exponents.

2.2. Spectrum of Lyapunov exponents

Lyapunov exponents (LEs) are an essential diagnostic tool for the stability of attractors and the presence of deterministic chaos in dynamic systems. They quantify the average exponential rates of divergence (or convergence) of neighboring orbits in phase space

[12]. An ordered set of LEs $\{\lambda_1, \lambda_2, \ldots, \lambda_n\}$ forms a spectrum where the cardinality of the set n matches the number of degrees of freedom of the system. If the system has at least one positive LE, the system is chaotic, and if we order the spectrum such that $\lambda_1 \geqslant \lambda_2 \geqslant \ldots \geqslant \lambda_{n}$, the maximal (largest) Lyapunov exponent is then $\lambda_{\max} = \lambda_1$. Moreover, if multiple exponents are positive, the dynamics are designated as *hyperchaotic* [36, 37].

To numerically estimate the exponents, a set of linearized equations with perturbed initial conditions is solved. If $u_i(t)$ are the particle trajectories, the perturbed trajectories $\delta u_i(t)$ are determined by the successive application, at each time step, of the linear propagators $J_{i,j}$ (the Jacobian) to the initial perturbed positions $\delta u_i(0)$ according to

$$\delta u_i(t) = \sum_j J_{i,j}(t,0)\delta u_i(0). \tag{4}$$

The finite-time LEs are defined as

$$\lambda_i(t) = \lim_{\|\delta\| \to 0} \frac{1}{t} \ln \frac{\|\delta u_i(t)\|}{\|\delta u_i(0)\|}, \tag{5}$$

and also represent the eigenvalues of the Jacobians. In our work, we examine the fluctuations of finite-time LEs around their converged (or 'asymptotic') limit and after the system has reached the steady-state dynamic regime.

To compute the LE spectrum, we employ the algorithm from [20], first proposed in [38, 39]. This particular algorithm was shown to be sufficiently accurate in the computation of the LEs and the associated eigenvectors for a multitude of systems, both conservative and dissipative [40].

As a criterion to determine when the LE spectrum is numerically converged, we take the following average relative error estimate

$$\frac{\delta\lambda(t_j)}{N} = \frac{1}{N}\sum_{i=1}^{N} \left| \frac{\lambda_i(t_j) - \lambda_i(t_{j-1})}{\lambda_i(t_j)} \right| < 5 \times 10^{-3}, \tag{6}$$

where $t_j = 5j\nu_0^{-1}$. This particular convergence criterion choice is made empirically by minimizing the trade-off between execution costs and precision. However, enforcing higher precision does not change our main results but rather changes the scale of the phenomenology we report on. In figure 2, we illustrate how the LE spectrum evolves and converges over time for a typical parameter set. In the top panel, we see that the individual exponents reach their 'asymptotic' values in a consistent manner which is captured by the relative error estimate $\delta\lambda/N$ (bottom panel). For the model under study, we performed the Gram–Schmidt orthonormalization of the linearized basis at every time step [20]. The difference between the usual application of local (finite-time) LEs and the way we calculated the exponents (see equation (6) for comparison in [41]) is that our evaluation interval is very short, i.e. of the same order as the time step we take. As we take the LE measurements in the steady-state dynamic regime, the evaluation interval can indeed be this short.

In the underdamped regime, the equations of motion are second order (see equation (3)), and to integrate them, we instead solve two sets of N first-order differential equations. Therefore, the size of the Jacobian matrix from equation (4) is
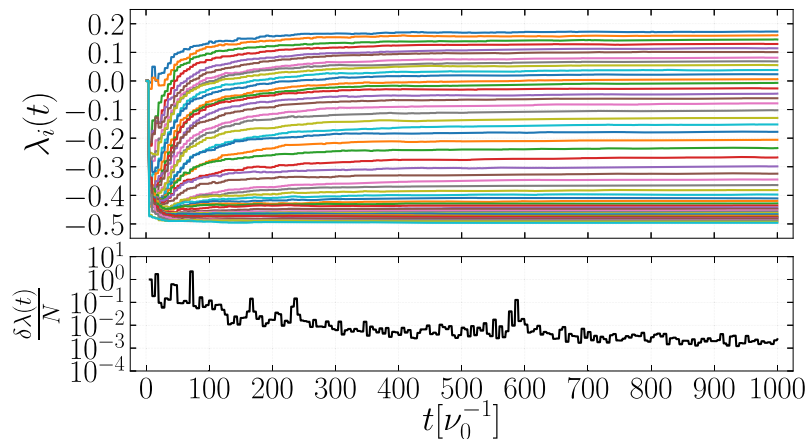
Figure 2. Time evolution of Lyapunov exponents $\lambda_i(t)$ (top) and from equation (6) the average relative error $\frac{\delta\lambda}{N}$ (bottom) for the dissipative driven FK model with parameters $N = 50$, $\omega = 1/2$, $F_{\mathrm{ac}} = 0.2$, $\nu_0 = 0.2$, $K = 4$, $m = 1$, $F_{\mathrm{dc}} = 0.17$.

$[2N + 1, 2N + 1]$, where the last equation is reserved for time. This amounts to the simultaneous solution of $(2N + 1) \times (2N + 1)$ linear and $2N + 1$ nonlinear first-order differential equations. In our study of the underdamped regime, we exclusively focus on the N largest exponents out of the total $2N$ number of exponents. In appendix A, we describe the motivation for this choice. However, in the strictly overdamped case, the total number of first-order equations (linear + nonlinear) is, instead, $(N + 2) \times (N + 1)$, which requires a separate implementation. Moreover, in this case, the particles are inertialess and half of the available phase space directions are neglected, making the total number of exponents N. We verified that by working with equation (3) and slowly approaching $m \to 0$ we can obtain the results of the strictly overdamped limit with a precision allowed by our integration routines (see also section 3 and figure 4).

The magnitude of the LEs measures the rate at which the system becomes unpredictable and how fast the information about the initial state gets scrambled [10]. The largest LE can be related to the reversibility of the dynamics and the Loschmidt echo, e.g. [42–44]. In the strictly overdamped limit of the FK model, the largest LE at vanishing DC driving was shown to be in close relation to the critical depinning force [30]. Moreover, in the JJ array systems, the critical depinning force is analogous to the critical current [34], therefore the study of the largest LE is of principal importance. By contrast, in the Kuramoto model, the characteristics of the LE spectrum are used to distinguish between different dynamic regimes [13]. Similarly, we identify GOE features (see sections 3.1, 3.2, 3.4 and 3.5) in the dissipatively driven FK model and show how we can identify several different dynamic regimes from the LE spectrum (see section 3.3).

3. Results

The fact that the dissipatively driven FK model exhibits hyperchaotic features, i.e. it is a dynamic regime with more than one positive LE, was already highlighted in [35]. In
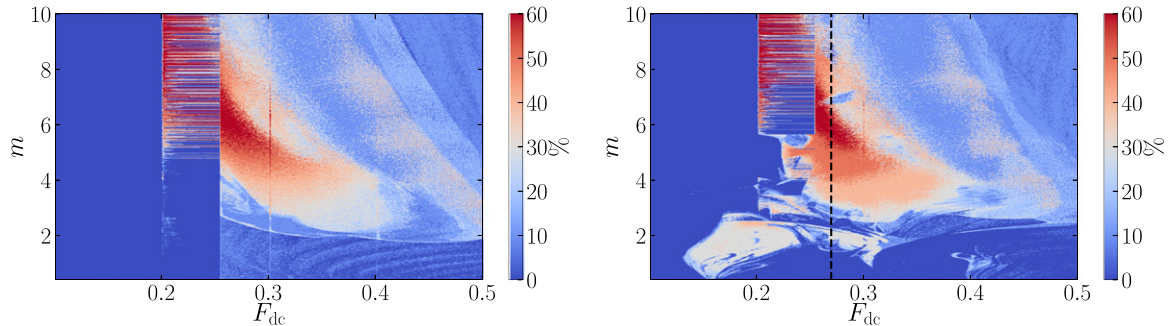
Figure 3. Percentage of positive LEs as a function of the DC force F_{dc} and the mass of particles m, for parameters $N = 10$, $\omega = 1/2$, $\nu_0 = 0.2$, $K = 4$. The force and mass step used are $\Delta F = 10^{-3}$ and $\Delta m = 5 \times 10^{-3}$, respectively. (Left) DC system with $F_{ac} = 0$. (Right) AC and DC system with $F_{ac} = 0.2$ where the vertical black dashed line is at $F_{dc} = 0.27$. The parameter regimes along the dashed line are examined later (see section 3.1).

this paper, we perform a deeper study of this interesting phenomenon and present new results related to the complex dynamic landscapes that emerge from this apparently simple model.

In figure 3, we show a heatmap of the results of a scan over the mass m and DC force parameter F_{dc}. By measuring the percentage of positive LEs in the spectrum, we can identify several different parameter regimes that lead to strongly chaotic dynamics. In the left panel, the results for a DC system ($F_{ac} = 0$) are shown, and in the right panel, those of an AC and DC system ($F_{ac} = 0.2$) are presented. In both cases, the dynamic landscapes exhibit large periodic phases (dark blue regions) with smaller chaotic windows (light blue to red regions).

We now additionally comment on the consistency of our calculations and numerical implementations. In particular, from [35], we know that whenever $\lambda_{max} > 0$ the system typically exhibits collective motion measured by the response function $\bar{v}$, which is defined as

$$\bar{v} = \langle\!\langle \dot{u}_i(t) \rangle\!\rangle_{T,N} = \lim_{T \to \infty} \frac{1}{TN} \sum_{i=1}^{N} \int_{t_s}^{t_s+T} \dot{u}_i(t) \mathrm{d}t \neq 0, \tag{7}$$

where t_s is the elapsed transient time, i.e. the time needed for the system to reach a steady state. Knowing this, we can be confident that our numerical integration of equation (3) and the LE spectrum computation in section 2.2 are correctly implemented. More specifically, we know that in the AC and DC strictly overdamped limit, the dynamic phase transition from the pinned regime to the sliding particle motion regime for the parameters specified in the captions of figure 3 happens at around $F_{dc} \sim 0.16$ [30, 31] (see also the top panel of figure 4). The results for the underdamped system in the right panel of figure 3 show that such a transition indeed happens in the $m \to 0$ limit where the chaotic patch shrinks towards this particular critical depinning force.

In both the DC-only case and the AC and DC case, a regime with strong intermittent chaotic behavior is present. Alternations between chaotic and periodic windows happen
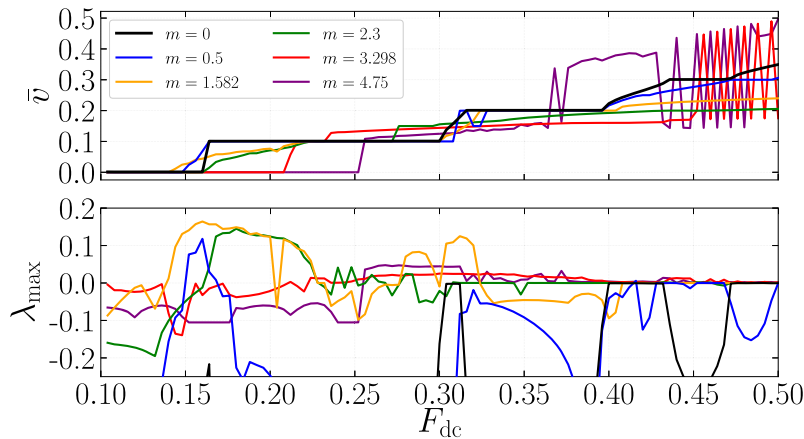
Figure 4. Average velocity $\bar{v}$ (top) and maximal (largest) Lyapunov exponent λ_{max} (bottom) as a function of the DC driving force F_{dc} for five different masses and the strictly overdamped limit. Parameters used: $N = 10$, $\omega = 1/2$, $F_{\text{ac}} = 0.2$, $\nu_0 = 0.2$, and $K = 4$ with a DC force step $\Delta F_{\text{dc}} = 4 \times 10^{-3}$.

for $0.2 < F_{\text{dc}} < 0.26$ with very small changes in the mass parameter. This means that the pinning-to-sliding transition in this model is more complex than previously thought. Therefore, going further with our analysis, we will focus on parameters that lead to dynamics deep inside the sliding regime where such intermittent behavior does not dominate the physics and stable phases are present, i.e. same-colored islands in the heatmap of figure 3. The AC and DC case exhibits larger and more robust islands. Due to this fact, the model that includes both AC and DC driving is the subject of our further investigation.

To illustrate the different dynamic regimes present in the driven FK model, in figure 4, we plot the response function $\bar{v}(F_{\text{dc}})$ (upper panel) and the largest Lyapunov exponent $\lambda_{\text{max}}(F_{\text{dc}})$ (lower panel). With a decrease in the mass parameter $m \rightarrow 0$, the response function and also the LEs converge towards the results for the strictly over-damped model and are consistent with the standard literature [31]. We note that we neglect any hysteresis effects in the response function by independently running the calculations for each particular F_{dc} [35].

We checked that for a larger driving frequency, e.g. $\nu_0 = 0.4$, the chaotic behavior is more pronounced, and the chaotic regions are larger. According to [45] and the author's work on the related model of a JJ array, chaotic behavior is only present within a particular frequency parameter window, and the size of this window is related to McCumber's parameter. Due to the obvious equivalence of the models, in our model, the size of this window is related to the mass m. Moreover, performing calculations for larger AC forces leads to hyperchaotic islands that are already present for smaller F_{ac}. Additionally, the coupling between junctions in the related model of JJ arrays has been shown to play an important role in inducing chaotic behavior [46].

To answer a commonly asked question regarding the commensurate dynamics of the FK model, a small particle number is typically used [15, 26]. More specifically, for fixed ω, $N \leqslant 10$ is shown to be sufficient to measure the system's response function $\bar{v}(F_{\text{dc}})$ and to establish whether the system is chaotic or not [17] (also see figure 4),
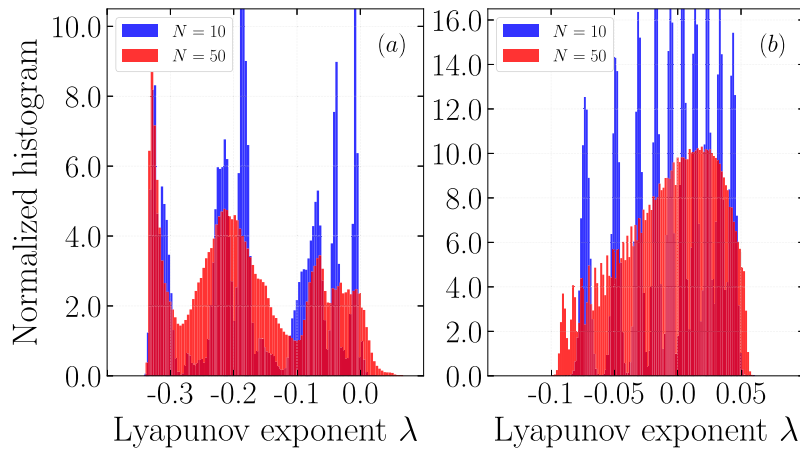
Figure 5. Histogram of the LE spectrum for different numbers of particles $N = 10$, 50 for a large number of realizations $M = 10^5, 10^4$, respectively. The number of histogram bins is 100. In (a), $m = 1.582$ and in (b), $m = 4.653$ while $F_{dc} = 0.27$ applies to both. The remaining parameters used are as stated in figure 4. Further details are given in section 3.1.

and these results would carry also over and be valid for $N > 10$ cases. However, deep inside the underdamped regime, the physics (for the considered system sizes) changes with the particle number. In particular, the percentage of positive LEs changes. Luckily, the change in the number of positive LE exponents with N is gradual. That is why we compute the heatmap with only $N = 10$, as presented in figure 3, with the expectation that similar (to within a few percent) chaotic content will be present in larger systems.

The presence of hyperchaoticity implies that information about the initial state of the system gets scrambled along with several directions in the phase space and the existence of a higher-dimensional attractor structure. The LE spectrum and its associated attractor are characterized by their fractal dimensions, correlation exponents, and information dimensions. Quantities such as the Kaplan-York dimension, which measures the information content of a dynamic model, can be computed. In addition, the sum of positive LEs is known to be related to Kolmogorov-Sinai entropy and the growth rate of entropy [20]. In this paper, we do not try to answer questions about information and entropy but rather focus on the statistics of the LE spectrum, which exhibit certain features of Gaussian random matrix ensembles [1–6].

To that end, we now comment on the consistency of the large degree of freedom limit $N \to \infty$ of this discrete model. Taking this limit is equivalent to an investigation of the perturbed sG equation itself. To achieve a reasonably 'smooth' LE spectrum distribution, a sufficiently large number of particles have to be employed. This is obvious from the plot of the LE spectrum histogram in figure 5 for an increasing number of particles N. For $N = 10$, the histograms and the corresponding distributions are not smooth enough to be compared to the explicit asymptotic results in RMT.

We already found that for $N = 50$, the LE spectrum contains all the main features which are present for much larger particle numbers with similar statistics. For example,
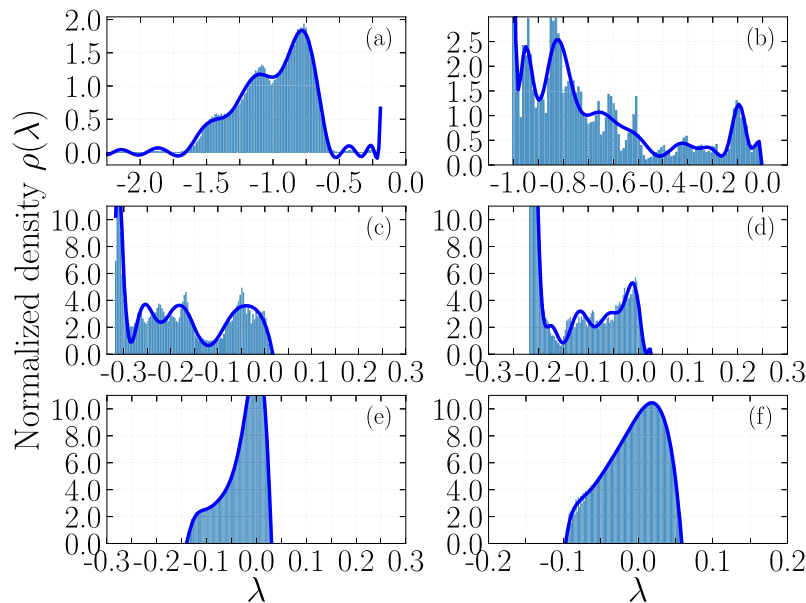
Figure 6. Normalized LE spectrum density at $F_{dc} = 0.27$, $\omega = 1/2$, $F_{ac} = 0.2$ and $\nu_0 = 0.2$ for different masses: (a) $m = 0$, $N = 400$, and $M = 790$; (b) $m = 0.5$, $N = 100$, and $M = 2265$; (c) $m = 1.582$, $N = 100$, and $M = 4607$; (d) $m = 2.3$, $N = 100$, and $M = 610$; (e) $m = 3.298$, $N = 100$, and $M = 4189$ and finally (f) $m = 4.75$, $N = 100$, and $M = 66\,370$. The corresponding averages are: (a) $\bar{\lambda} \simeq -0.995$, (b) $\bar{\lambda} \simeq -0.684$, (c) $\bar{\lambda} \simeq -0.177$, (d) $\bar{\lambda} \simeq -0.133$, (e) $\bar{\lambda} \simeq -0.026$, and (f) $\bar{\lambda} \simeq -0.006$. The dark blue lines are the fits obtained via equation (8) and each one represents the probability density function (PDF) of the respective spectrum. The number of histogram bins is 100.

in figure 5, only small fluctuations around the left tail of the distribution can be observed when the particle number is doubled. These fluctuations influence the output of the unfolding procedure discussed in section 3.2, but the cost of integrating a system with N degrees of freedom and $2N$ dynamic variables scales according to $\sim N^2$ and the added precision does not warrant the steep computational cost. Therefore, for our scientific purposes of pointing out the similarities between the LE spectrum of a dissipative system and RMT ensembles, a lower precision can be justified. Nevertheless, in the following, to decrease the finite-size effects even further, we typically use $N = 100$ particles.

3.1. Normalized Lyapunov spectrum density

In figure 6, we present the results for the normalized LE spectrum as a function of the mass term m. We fix the driving force at $F_{dc} = 0.27$ and $N = 100$ and the remaining parameters are set to the values given in the captions of figure 3 (except for the strictly overdamped limit, for which $N = 400$). For this parameter choice, the system exhibits a collective motion $\bar{v} \neq 0$, as can be observed in the upper panel of figure 4.

The histograms (blue rectangles) in figure 6 are generated for a large number of realizations M at $t = 0$, and after the system has reached the steady state and fulfilled the convergence criterion from equation (6). The initial conditions are chosen such that

the particle positions have a Gaussian distribution with a mean $\mu = N/2$ and a standard deviation σ is selected such that the particles symmetrically fall into the domain $[0, N\omega]$. Additionally, the initial velocities of the particles are set to be equal to zero. Drawing the initial particle positions from a uniform distribution in the same domain yields equivalent results for the LE spectrum.

The dark blue lines in the figures represent the fit of the histogram data to a higher-order polynomial

$$\rho(\lambda, \bar{\lambda}) = \sum_{k=0}^{k_{\max}} a_k (\lambda - \bar{\lambda})^k, \tag{8}$$

where $k_{\max}$ is chosen based on the details of the spectrum. In particular, the more local maxima the distribution has, the larger the $k_{\max}$ that is required. For example, for $m = 4.75$ depicted in figure 6(f), the choice $k_{\max} = 10$ accurately approximates the distribution [11]. The fit is centered around $\bar{\lambda}$ which is defined as the ensemble average

$$\bar{\lambda} = \langle\langle \lambda_{i,j} \rangle\rangle_{N,M} = \frac{1}{NM} \sum_{j=1}^{M} \sum_{i=1}^{N} \lambda_{i,j}, \tag{9}$$

where j specifies the initialization. The fitted lines do not capture the extremely detailed structure of the spectrum for smaller masses, e.g. (b) and (c) in figure 6. This influences the unfolding procedure we use in section 3.2. However, for the most interesting cases such as (a) and (f), this imprecision does not play a role.

With an increase of m and for fixed F_{dc} (along the vertical dashed line in the right panel of figure 3), the normalized LE spectrum undergoes a transition from a regime where all the exponents are negative, to a regime where half of the spectrum is positive. From figure 6, it can be seen that the normalized LE spectrum does not follow any characteristic function or rule other than slowly moving to the positive domain for an increasing mass term. For the particular island (a dark orange patch in the heatmap) with roughly fifty percent of positive LEs where $\bar{\lambda} \to 0^-$, we observe a distribution that resembles a semi-circle law. This is also nicely illustrated in figure 5(b) for the case $N = 50$.

Similar findings, but in conservative models, have been reported in [10, 13], where the authors make a connection between the LE spectrum and RMT. They identify the semi-circle law which is symmetric around $\bar{\lambda} = 0$ and which, under appropriate rescaling, matches the semi-circle law and that of GOE [6]. We argue that in a dissipative dynamic model such as the underdamped FK model, the features of GOE are present, even though we are not able to fit our results to the semi-circle due to dissipation that forces the spectrum to have a negative mean. In the following sections, we use diagnostic tools common in the RMT literature to do so.

3.2. Normalized Lyapunov spectrum spacings

Conventionally, in the study of RMT and related problems, the nearest-neighbor spacing distribution is generated from the eigenvalue spectrum. Rather than the eigenvalue spectrum density, the distribution of eigenvalue spacings is typically regarded to be

universal [4]. For our particular purposes, it is sufficient to present the following relevant PDFs:

$$P_{\text{Poisson}}(s) = \mathrm{e}^{-s} \qquad \text{uncorrelated,} \tag{10}$$

$$P_{\text{GOE}}(s) = \frac{\pi s}{2} \mathrm{e}^{-\frac{\pi}{4}s^2} \qquad \text{correlated,} \tag{11}$$

where similar expressions exist for the remaining correlated Gaussian ensembles [47]. Equation (11) is recognized as Wigner's surmise in the RMT literature, while equation (10) is the well-known Poisson distribution.

LEs can be viewed as eigenvalues that characterize chaotic, periodic, and quasiperiodic motion [14, 48]. Therefore, by treating them as such, the corresponding PDF can be computed. In our case, $P(s)$ represents the probability density that two consecutive LEs have a spacing of s, and, like any PDF, it is normalized to unity. Typically, the spacings represent an order set of

$$\tilde{s}_{i',j} = \lambda_{i'+1,j} - \lambda_{i',j}, \tag{12}$$

for the realization $j = 1, 2, \ldots, M$. In practice, the LE spacing PDF is obtained from the normalized histogram of $s_{i',j}$ values as

$$s_{i',j} \equiv N \cdot \left(R(\lambda_{i'+1,j}, \bar{\lambda}) - R(\lambda_{i',j}, \bar{\lambda}) \right), \tag{13}$$

where $i' = 1, 2, \ldots, N - 1$ and with the help of the cumulative spacing distribution $R(\lambda, \bar{\lambda})$ defined as

$$R(\lambda_{i',j}, \bar{\lambda}) = \int_{\bar{\lambda}}^{\lambda_{i',j}} \rho(\lambda') \mathrm{d}\lambda'. \tag{14}$$

In the RMT literature, this particular way of computing the spacing PDF is known as the 'unfolding' procedure. The unfolded LE spectrum, computed using equation (13), can now be directly compared to equations (10) and (11), and the results are presented in figure 7. Note the difference between the definitions of s and $\tilde{s}$.

In the strictly overdamped regime (see figure 7(a)), the unfolded spectrum histogram is consistent with a Poisson distribution. Small fluctuations exist, but the LE spectrum spacings in the $s \to \infty$ limit convincingly follow equation (10). However, to achieve this identification, a large number of particles ($N = 400$) had to be used to obtain an LE spectrum that was sufficiently smooth. With a further increase in the particle number, we expect the spacing spectrum to move progressively closer and closer to the Poisson distribution, as it already showed this tendency for $N < 400$ with increasing N. We further comment on the physics of this regime in section 3.3.

In the underdamped regime and for $m = 0.5, 1.582, 2.3$, the unfolded separation distribution does not follow Poisson's law or Wigner's surmise; see figure 7(b)–(d). For $m = 0.5$, the system exhibits similar periodic behavior to that of the $m = 0$ case, and this is the reason why, for $s > 2$, the separations between LEs appear to have a Poisson distribution. We checked that regions with similar levels of chaos conform to similar
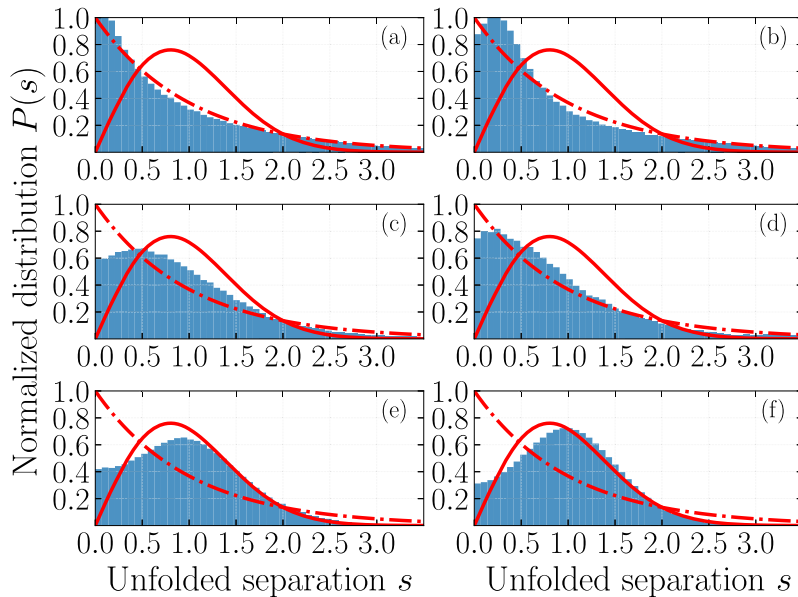
Figure 7. The unfolded LE spectrum histograms obtained using equations (13) and (14). The parameters used in the simulations are the same as in figure 6. The red dashed line is the Poisson distribution and the full line is Wigner's surmise, described by equations (10) and (11), respectively. Further details are given in the text.

distributions, i.e. regions with the same color in the heatmap in figure 3 have equivalent LE spectra and spacings.

As the mass is increased, the system enters hyperchaotic regimes. In figure 7(e), we observe a distribution depletion in the $0 < s < 1$ range, which signifies that repulsion between the LEs occurs. LE repulsion was first observed in [14], in a conservative model which was used to describe a periodically kicked rotator. In the parameter regime where this model exhibits hyperchaos, the act of coupling between nearest-neighbor standard maps introduces LE repulsion. Before coupling, this model was already hyperchaotic but did not exhibit any LE level repulsion, hinting at the fact that coupling plays an extremely important role in generating a spectrum that exhibits *correlated* RMT ensemble features. In the same paper, the authors mentioned that dissipative models also exhibited similar behavior, but in our work, we provide explicit evidence for this. In the dissipatively driven FK model, the coupling between particles is the nearest neighbor and is not treated as a parameter (see equation (3)). Therefore, any hyperchaotic behavior within such a model is expected to exhibit LE repulsion.

For $m = 4.75$ in figure 7(f), the unfolded spectrum has an even stronger repulsion as $s \to 0$, compared to the other sampled cases. This parameter point sits in the already mentioned hyperchaotic regime and has roughly 50% positive exponents (the dark orange region in figure 3). In this case, $P(s)$ follows the Wigner surmise perfectly for $s > 2$, indicating that this distribution is more similar to equation (11) than (10). The maximal height of the distribution matches that of the GOE as well, but it is shifted to the right. We attribute the lack of a persuasive overlap to the dissipative dynamics

that force the LE spectrum to have an asymmetric distribution. The fact that the phase space volume is not conserved through time evolution leads to this shifted peak in the unfolded spectrum. We take this as an indication that, in the dissipative system, the LE spectrum might be not described by a pure GOE ensemble but rather by an ensemble mixture of GOE and Wishart ensembles [6]. We can observe an additional hint of this in figures 6(e) and (f). In particular, the left tail of the normalized density $\rho(\lambda)$ shows similar behavior to the Marchenko–Pastur law [6, 8].

The lack of strong LE repulsion as $s \to 0$ cannot be exclusively attributed to the dissipative nature of the dynamics in our study. Inspecting the LE spectrum in more detail, we often observe pairs of LEs to be present. These exponents are equivalent up to two or three decimal digits and continue to be so with an increase in the system size N. This kind of 'near degeneracy' has also been observed in chains of Rössler oscillators and is attributed to the (discrete) translational symmetry of the model [21]. Similarly, we argue that, due to this fact and the inherently fluctuating nature of finite-time Les, the Lyapunov vectors tend to align in the same directions in phase space, producing near degeneracy and ultimately a lack of complete LE repulsion. This is typically thought to be a spurious and subtle problem of numerical accuracy in the method used to obtain the LEs. For a definite and consistent analysis, the Lyapunov vectors have to be computed. This kind of analysis would also potentially explain why, in the conservative system of coupled Kuramoto oscillators, similar features are present, see figure 4 of [13]. Conversely, for an explanation of why and how these features are not present in the classical D0-brane model, see figure 1 [11].

3.3. Particle trajectories

In previous studies of the dissipatively driven FK model, the particle trajectories provided valuable information about the presence of chaos. Insight into the spatiotemporal dynamics of the system is used, for example, in [49], to supplement the use of common tool such as LEs for chaos detection.

In figures 8(a)–(c), we plot the particle trajectories over time for different particle masses in the moving reference frame for visual clarity. A moving frame is used because the system is in the sliding regime where the particles exhibit collective motion related to the AC and DC driver, see figure 4. In the remaining figures of figures 8(d)–(f), the corresponding LE spectrum is presented.

When the system is in the strictly overdamped regime ($m = 0$), i.e. when the inertial term is negligible in comparison to the damping term, individual particles act as impenetrable hard spheres. In figure 8(a), this is depicted clearly, where, in the steady-state regime, each particle feels the neighboring particles but they never exchange places and break the ordering at the initial time. Even in the transient regime, the particle order is preserved. To specify when two particles trajectories cross and particles break the initial time ordering, we used red crosses, and no red crosses are shown in the strictly overdamped regime. This is because, in this regime, the physics of the model is subject to Middleton's no-passing rule [50].

Middleton's no-passing rule refers to the order-preserving nature of the underlying dynamics in the presence of convex interparticle interactions and is extensively exploited to gain analytical insight into complex dynamics [27]. Under such an assumption, if two
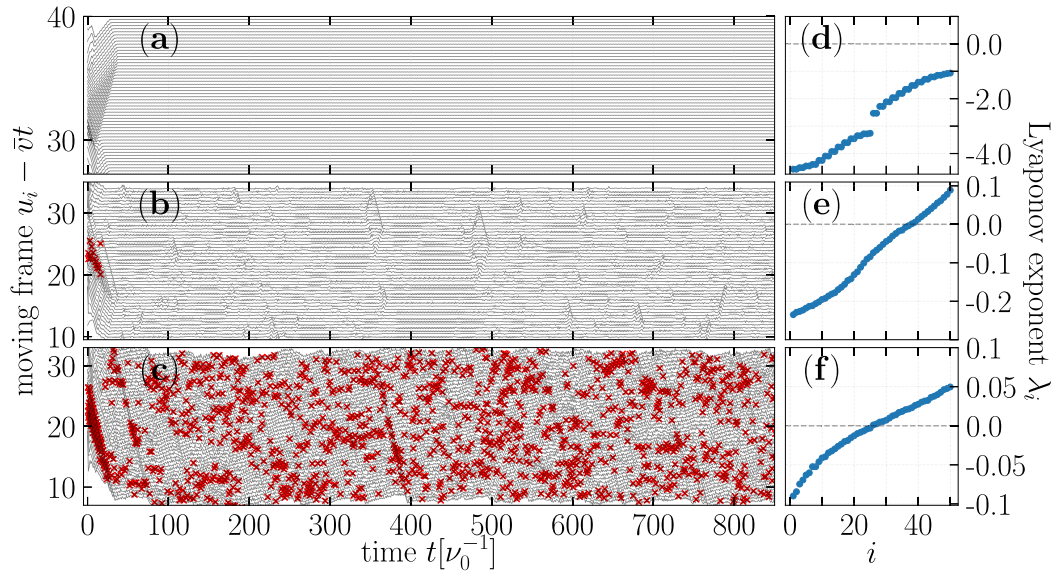
Figure 8. A single realization of particle trajectories for different mass parameters: (a) $m = 0$, (b) $m = 2.047$, and (c) $m = 4.653$ at a fixed DC force $F_{\mathrm{dc}} = 0.27$; the remaining parameters are as defined in figure 2. The trajectories are plotted in the moving frame (sliding regime), for visual clarity. We used the periodic boundary conditions mentioned in section 2.1. Red crosses denote the occasions when particles break the initial time ordering.

configurations are initially ordered $u = (u_i)_{i \in \mathbb{N}}$ and $\tilde{u} = (\tilde{u}_i)_{i \in \mathbb{N}}$, e.g. $u \leqslant \tilde{u}$ (where $\leqslant$ refers to each particle position $u_i \leqslant \tilde{u}_i \forall\, i$) then this ordering persists through time evolution [51]. This means that the system does not evolve towards less complexity than it already possessed at the initial time. In [30], it was argued that this rule is related to the absence of chaotic behavior. We now provide further evidence that this is indeed the case and additionally claim that it leads to Poissonian statistics in the LE spectrum. Explicit evidence can be found in figures 6(a), 7(a), and 8.

Intuitively, in the strictly overdamped regime, the 'avoided crossing' behavior of particle trajectories leaves less phase space for each of them to explore. This restricted phase space means that LEs are left with less variability and therefore the exponent values can and must be close together (but are not degenerate). This is nicely illustrated by the unfolded LE spectrum $P(s)$ of figure 7(a) as $s \to 0$. In the underdamped regime, the available phase space is larger and LEs have inherently larger separations between them, which thereby justifies LE 'repulsion', i.e. the suppression of the $P(s)$ weight when $s \to 0$; see, e.g. figure 7(f).

In the underdamped regime, due to the presence of the inertial term, the particles can overcome the harmonic interparticle repulsion and exchange positions. This is shown in figures 8(b) and (c), for which the corresponding LE spectra are given in (e) and (f). Different chaotic regimes can be identified in figure 8(b), compared to (c). First, one where the crossings only happen in the transient regime and the second where such crossings can propagate through time and are present even in the steady-state regime. The latter is the regime with roughly fifty percent positive LEs (the dark orange region

in figure 3) and where LE repulsion is prevalent. We note that after exchanging positions, particles quickly revert to the previous ordering due to the overwhelming strength of the particle interactions. We checked that when different initial conditions are chosen, e.g. uniformly distributed particle positions, the transient dynamics looks different, but in the steady state, the general conclusions provided are still valid. This means that the LE spectrum and the LE fluctuations are completely determined by the nonlinear dynamics rather than by the choice of initial conditions.

In the literature, the term 'avoided crossing' is typically used to describe the repulsive behavior of eigenvalues in quantum mechanical models with the change of some control parameter [21]. Similar behavior, as already mentioned, has been used in the context of LEs [14]. Note that the avoided crossing behavior discussed so far in this chapter is in terms of particle trajectories. We identify a dichotomy, where the lack of avoided crossings in the trajectories leads to avoided crossings in the LEs (exponent repulsion) and vice versa.

Within the paradigm of the FK model, the particle trajectory crossing behavior might appear to be nonphysical, as, due to its finite size, any classical object would forbid it. However, in this regime and under the following variable changes $2\pi u_i = \varphi_i, m = K = a^2, m\alpha = 1, mI = 2\pi F_{dc}, mA = 2\pi F_{ac}, \omega = 2\pi\nu_0$ the dissipatively driven AC and DC FK model directly maps to the realistic model of Josephson transmission lines in a stripline geometry [52, 53]. This type of model can capture quantum phenomena that occur in JJ systems despite being considered as classical in essence [15, 19]. In the JJ array models, φ_i represents the phase jump of the wave function across a single junction, and therefore, in this particular context, there is no ambiguity in the crossing behavior, as it simply implies that phase order is violated.

3.4. Consecutive Lyapunov exponent spacing ratio

To supplement the standard tools that uncover the RMT statistics, such as the normalized density in section 3.1 and the spectrum unfolding in section 3.2, we compute the average consecutive spacing ratio $\bar{r}$. This ratio is defined as

$$\bar{r} = \left\langle \left\langle \frac{\min\left(\tilde{s}_{i',j}, \tilde{s}_{i'+1,j}\right)}{\max(\tilde{s}_{i',j}, \tilde{s}_{i'+1,j})} \right\rangle \right\rangle_{N-2,M}, \tag{15}$$

where $\tilde{s}_{i',j}$ is as defined in equation (12). First, the average is taken over $N-2$ consecutive spacing values, then additionally over M samples. The consecutive spacing ratio does not require unfolding and allows for a more transparent comparison between RMT ensembles and experimental/simulated datasets [54]. In the study of quantum many-body localization, where an extremely large number of realizations is computationally expensive to realize, the consecutive level spacing ratio PDF $P(r)$ was shown to provide more precise results than the common spacing distribution, $P(s)$ [55]. The average consecutive spacing ratio is independent of the local density of states and is therefore a more suitable diagnostic tool than the unfolded spectrum in cases where the number of ensemble realizations is limited. This happens, as mentioned, in quantum
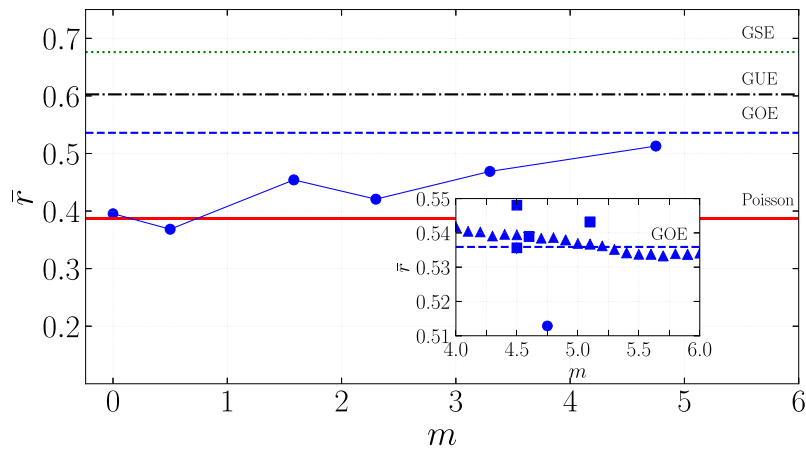
Figure 9. Consecutive LE spacing ratio $\bar{r}$ (blue circles) for the different mass parameters used in figures 6 and 7. The lines between the values are guides for the eye. The explicit expressions for the GUE and GSE ensembles are given in [54], while the values for the Poissonian and GOE ensembles are given in the text. The inset shows the $\bar{r}$ for different masses along the $F_{dc} = 0.27$ line (triangles), and other randomly chosen parameter points in the hyperchaotic region with roughly $\sim 50\%$ percent positive LEs (squares). The inset data has been generated for $N = 50$ and $M \sim 10^4$. A discussion of the inset and the figure is given in the text.

many-body problems where sampling of the eigenspectrum is limited due to the exponentially increasing Hilbert space dimension, or in our particular case, where we flow $\sim N^2$ differential equations to obtain the LE spectrum of N exponents.

In figure 9, we present the results for the particular six points in the parameter space and statistics that were already the subject of investigation in sections 3.1 and 3.2. In the strictly overdamped regime, the ratio $\bar{r}$ is consistent with the analytically predicted value $2\ln 2 - 1$ that corresponds to a Poisson distribution. In the underdamped regime and with an increase in the mass, the consecutive LE spacing ratio slowly moves closer to $4 - 2\sqrt{3}$, which corresponds to the GOE ensemble prediction [54].

In the inset of figure 9, we present the results of $\bar{r}$ for multiple points in the parameter region with roughly $\sim 50\%$ percent positive LEs, i.e. parameter points in the dark orange region in figure 3. The consecutive LE spacing ratio consistently shows agreement with the GOE ensemble. In this check, we used $N = 50$ to generate enough samples for a reliable evaluation. However, some points lie close to, or on top of, the GOE expectation, which, after close examination of the unfolded spectrum, does not fully show compliance with the expression for Wigner's surmise. These results provide a false positive argument for a complete overlap with the GOE, and should be used to state that the underlying LE spectrum is close to, but surely not identical to the GOE due to dissipation, finite-size effects, and insufficient statistics.

3.5. Distribution of the largest Lyapunov exponent

Finally, we discuss the largest LE $\lambda_{\max}$ fluctuations in the hyperchaotic regime with roughly 50% positive exponents. In common examples of chaotic dynamic systems, the

distribution of individual finite-time LEs follows a Gaussian distribution [56] while, for example, in the presence of intermittent chaos, this distribution has been shown to be non-Gaussian [57]. In the following, we argue that, due to the presence of LE level repulsion (see figure 7), the fluctuation statistics of the $\lambda_{\max}$ show a behavior similar to the Tracy–Widom (TW) distribution [58]. The TW distribution, in effect, is a Gaussian distribution that is skewed and which has particular left and right decaying tails. Before we present the results we obtained by using sensitive numerical indicators for the presence of the TW distribution, we first briefly present its definition. The largest eigenvalue statistics of an $[N \times N]$ GOE approaches the TW CDF as

$$F(\lambda) = \lim_{N \to \infty} \text{Prob} \left(\left(\lambda_{\max} - \sqrt{2\,N} \right) \left(\sqrt{2} \right) N^{1/6} \leqslant \lambda \right). \tag{16}$$

For a transparent comparison between the eigenvalue statistics of RMT and TW, see, e.g. [59].

The fluctuation statistics of the largest/smallest eigenvalue of a random matrix around its mean follows the TW distribution and since this was discovered, it has been demonstrated that it plays an important role in many diverse fields such as mathematical physics, directed polymer physics, random growth models, finance, etc [60–62]. For example, in experiments of interface growth in thin films [63] the interface height fluctuation statistics have shown to be in accordance with the solution of the Kardar–Parisi–Zhang (KPZ) equation, which is precisely the TW distribution [64]. Depending on whether the growing interface is flat or curved, different universality classes such as GOE and GUE were observed to be present, respectively. In the context of RMT, the TW distribution successfully captures the crossover between two different phases present in the eigenspectrum. In particular, the eigenvalues of an RMT ensemble that follows the semi-circle law behave differently in the bulk compared to the edges of the spectrum. The left tail of the TW distribution describes the 'strong' coupling regime of the bulk and the right tail the 'weak' coupling regime present at the spectral edges [65].

From figure 6(f), the right spectral edge of the LE spectrum in the regime with 50% positive exponents appears to have finite support and to be consistent with the semi-circle law. Moreover, several spatially extended dynamic systems with their respective Lyapunov exponents and vectors have been found to fall inside the KPZ class [21]. Therefore, naturally, we investigate whether the distribution of $\lambda_{\max}$ in the dissipative and AC- and DC-driven FK model is distributed in accordance with the TW distribution. In this respect, we do not settle for simply superimposing the fluctuation histograms of $\lambda_{\max}$ and the TW PDF, but rather investigate this question using the following robust measures.

To reduce statistical noise and minimize small dataset sampling bias (present in any finite dataset such as our LE spectrum data) we average the statistical observables in the following way

$$\langle A\left[\lambda_{\max}\left(M'\right)\right]\rangle_P = \frac{1}{P}\sum_{p=1}^{P} A\left[\lambda_{\max}\left(M'_p\right)\right] \tag{17}$$
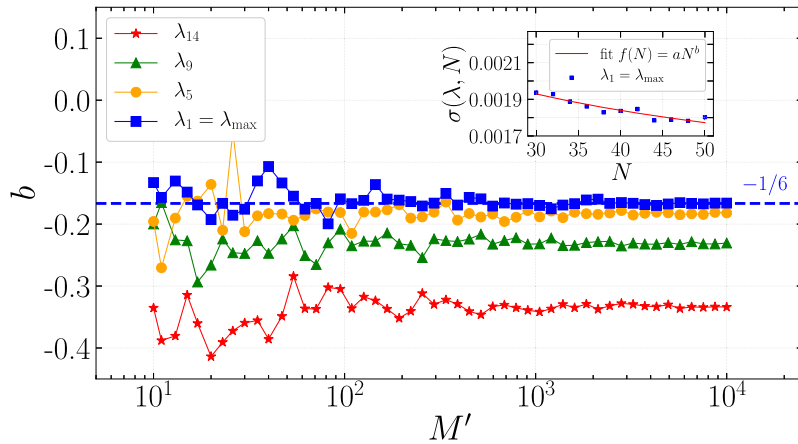
Figure 10. Scaling exponent b of the underlying fluctuation distribution for different ordered Les plotted against an increasing number of simulation averaged realizations M' with $P = 50$. To reduce the graphical clutter, we chose to present LEs significantly far apart in the spectrum. The expected spectral edge fluctuations of $b = -1/6$ according to RMT are plotted in a straight dashed blue line for comparison. In the inset, the standard deviation of the largest LE data is fitted for $M' = 10^4$ and changing numbers of particles N for the largest LE $\lambda_1 = \lambda_{\max}$. The fitting parameters obtained are $a = 0.00339496(5)$ and $b = -0.1661(4)$. The remaining simulation parameters are: $F_{dc} = 0.27$, $m = 4.653$, $\omega = 1/2$, $F_{ac} = 0.2$, and $\nu_0 = 0.2$. The data points for the main frame are generated by performing regression analysis as depicted in the inset.

where A denotes the observable of interest and M'_p is the size of the p'th subset of the total dataset of size M. We sample $M' \leqslant M$ values $p = 1, 2, \ldots, P$ times and finally an average is taken. Calculating averages using equation (17) is only beneficial in the case of small M', and in case of large enough M, these averages should give the same output.

In figure 10, we present the results for the standard deviation σ of the distribution of the largest LE and a few other LEs in the bulk. We find that with sufficient sampling, $\lambda_1 = \lambda_{\max}$ fluctuates in the spectral edge, in accordance with the expectations of RMT (the dashed blue line). In the inset, we show that for the largest M', the measured σ in the LE spectrum follows the fitting function $f(N) = aN^b$, where a is a trivial scaling parameter and b is the power-law exponent. The observed scaling of the fluctuations, which follows $-1/6$, is consistent with the TW distribution. Furthermore, the LE λ_k, $k \geqslant 1$ fluctuations away from the edge exhibit the same trend as that present in GOE bulk eigenvalues, i.e. movement toward $N^{-1/2}$ spectral bulk scaling.

It is important to note that, in generating the datasets required for the analysis in figure 10, with the change of the particle number N in the dissipative and driven FK model deep inside the underdamped regime, the physics changes a bit as well. In particular, the average percentage of positive LEs changes when the system size is increased in this way. Therefore, a simple scan over different N to obtain σ invites caution. Fortunately, when the remaining model parameters are fixed (see the caption of figure 10) and for the selected Ns, the percentage fluctuation of positive LEs is less than 1%.
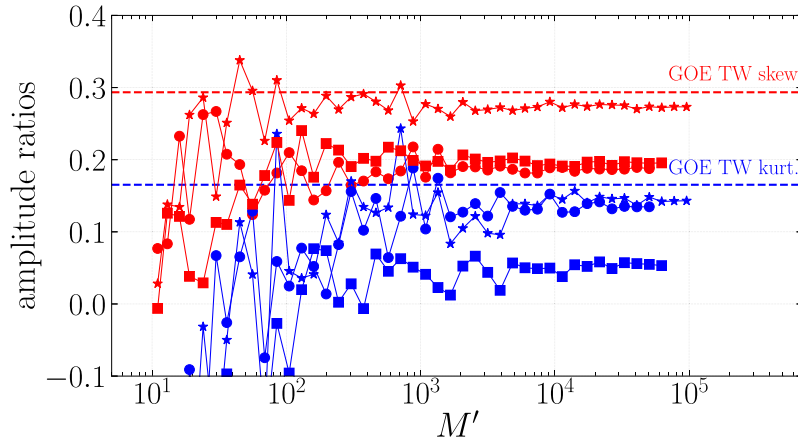
Figure 11. The skewness (red) and the excess kurtosis (blue) of the largest LE distribution for $N = 50$ (circles) and $N = 100$ (squares). We consider $m = 4.653$, $M = 53\,658$ for the $N = 50$ case and $m = 4.75$, $M = 66\,370$ for the $N = 100$ case, while the DC drive is fixed at $F_{\mathrm{dc}} = 0.27$; with these parameters, the system is in the hyperchaotic regime, with half of the LEs positive. The remaining parameters are given in the caption of figure 6. The straight dashed lines are the skewness and excess kurtosis of the GOE TW distribution. For comparison, we present the results of a single $M = 10^5$ sampling of the largest eigenvalue of random GOE matrices (stars) for $N = 100$. The number of subsequent averages taken is $P = 50$.

In figure 11, we compute the skewness and excess kurtosis which measure the asymmetry of a PDF about its mean and its 'tailedness,' respectively. These kinds of measures provide a test for the presence of the TW distribution, e.g. see [64]. We employ Pearson's second skewness coefficient and the coefficient of excess kurtosis defined as

$$\mathrm{Skew} = \frac{3\left(\langle \lambda_{\max} \rangle_{M'} - \Lambda_{\max}\right)}{\sigma}, \tag{18}$$

$$\mathrm{Kurt} = \frac{\frac{1}{M'}\sum_{j=1}^{M'}\left(\lambda_{\max,j} - \langle \lambda_{\max} \rangle_{M'}\right)^4}{\left[\frac{1}{M'}\sum_{j=1}^{M'}\left(\lambda_{\max,j} - \langle \lambda_{\max} \rangle_{M'}\right)^2\right]^2} - 3, \tag{19}$$

where σ defines the standard deviation and $\Lambda_{\max}$ is the sample median [66]. The observed skewness and excess kurtosis for the distribution of the largest LE are not in complete agreement with the expected values for the TW distribution. Nevertheless, both measures have a statistically significant trend of having positive values. Furthermore, the skewness shows a consistent tendency to move closer to the TW skewness with increasing N, while this is not the case for the excess kurtosis. This is because excess kurtosis quantifies the behavior of the decaying tails of a given distribution and can only be improved by sampling rare events, which, in turn, requires numerical effort at a significantly larger scale than the one we were able to perform. We note that the characteristic skewness and the shape of the tails of the largest GOE eigenvalue distribution (which is known to follow an asymptotic TW distribution) are numerically difficult to obtain using finite N and straightforward sampling. This can be seen in figure 11,

where the star-shaped data points represent such an attempt. In this case, the correct asymptotic skewness and excess kurtosis have been extracted from [67] using specialized techniques.

4. Conclusions

In this paper, by studying the Lyapunov exponent fluctuations, and treating the exponents as eigenvalues that characterize the nature of the classical dynamics (chaotic, quasi-periodic, and periodic), we provided numerical evidence for the existence of level repulsion akin to the RMT GOE ensemble in the AC and DC dissipatively driven FK model. The normalized Lyapunov exponent spectrum, Lyapunov exponent spacings, and consecutive Lyapunov exponent spacing ratio consistently indicate the presence of both *uncorrelated* and *correlated* statistical features in this model. Furthermore, an extensive numerical study of the large parameter space revealed rich and varied dynamic phases. In the strictly overdamped regime (when particle masses $m \to 0$) the particle trajectories show an 'avoided crossing' behavior, whereas deep inside the underdamped regime and for a particular parameter set, we identified persistent trajectory crossing behavior. We showed that these two regimes have Poissonian and almost Wigner GOE distributed Lyapunov exponent spacings, respectively.

Our research is a step towards potentially explaining why classical dynamic models, such as JJ array models subjected to external radiation (which represent related systems to the dissipatively driven FK model), can capture quantum phenomena so well [15, 19, 29, 52]. In particular, the underlying statistics (Lyapunov exponents in classical, and eigenvalues in the quantum case) seem to be guided by the same universal features. This opens a new and interesting direction in this and related fields of research.

Furthermore, the identification of Poissonian statistics in the particular limit of the strictly overdamped regime of the FK model gives hints to the potential presence of integrable structures in the continuum limit of the damped and driven perturbed sine-Gordon equation [25]. However, the particular role of the Lyapunov exponents and their relation to integrability requires further investigations, which were performed in, e.g. [68], for eigenvalue spacings in the quantum models. We conjecture that the presence of uncorrelated statistics is a general feature which means that *in any strongly coupled overdamped system (with a sufficiently large number of degrees of freedom) where Middleton's no-passing rule applies, the spectrum of LE spacings has Poissonian statistics*. Moreover, in quantum many-body problems, the presence of Poissonian statistics implies the existence of an infinite number of conservation laws, which typically leads to an exact solution that uses the Bethe ansatz technique. Therefore, it would be interesting to explore the contingency of our results on the existence of integrability in the quantized version of the strictly overdamped version of the FK model, if such a model can consistently be constructed.

An interesting aspect of the hyperchaotic regime with $\sim 50\%$ positive LEs is the presence of breathers. Examining the trajectories in more detail reveals the presence of short-lived collective (involving more than one particle) excitations that appear to mediate the particle crossings. From figure 8(f), this dynamic mechanism is not obvious

and a more careful study, such as that of [69], of this interesting phenomenon and its relation to LEs is required.

The main challenge we faced in this line of research was obtaining sufficient statistics for the Lyapunov spectrum fluctuations for a reliable comparison with the asymptotic results of the Gaussian random ensembles. In this paper, we extensively discussed this fact and showed how, for the examined model, we had to solve $\sim N^2$ differential equations in the strongly nonlinear and chaotic regime (N is the number of particles) to determine the spectrum. Interestingly, thanks to the sophisticated diagnostic tools developed in the literature, even with finite N and a modest number of realizations M^c we were able to capture the main features which are extremely close to the prediction of the Gaussian random matrix ensembles in the limits $N \to \infty$ and $M \to \infty$. Moreover, we presented hints that the largest Lyapunov exponent fluctuations for a particular parameter regime behave according to the famous Tracy–Widom distribution. Therefore, an imperative future research direction is the application of efficient algorithms to investigate whether this is indeed the case and how the different degrees of hyperchaos that are present in the model influence the behavior of the largest Lyapunov exponent.

Acknowledgments

Appendix A. Discussion of the total Lyapunov exponent spectrum

In this appendix, we discuss the total Lyapunov exponent spectrum measured for the considered variant of the FK model in the underdamped regime. More specifically, we present the results for the full spectrum of $2N$ exponents instead of the N largest exponents used in the main text.

From figure A1, we observe that the spectrum of the remaining N exponents (not displayed in figure 6) presents a mirror image of the spectrum of the largest N exponents, implying equivalent exponent spacing statistics. We note that considering only the first N largest exponents for a large enough ensemble already provides sufficient data for our claims. For more details on the notations and parameters mentioned in the captions of figure A1, please see section 3.
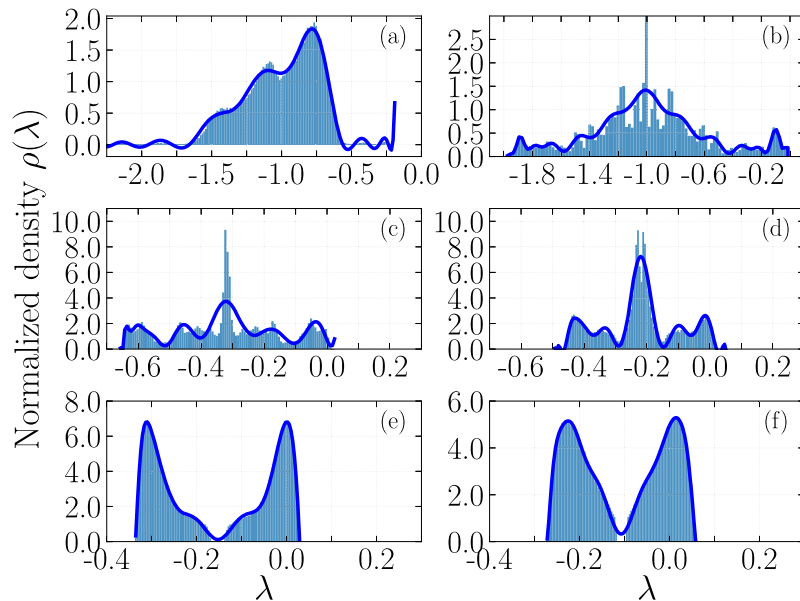
Figure A1. Normalized total LE spectrum density of $2N$ exponents at $F_{\mathrm{dc}} = 0.27$, $\omega = 1/2$, $F_{\mathrm{ac}} = 0.2$, and $\nu_0 = 0.2$ for different masses: (a) this figure is the same as in figure 6(a) $m = 0$, $N = 400$, and $M = 790$; (b) $m = 0.5$, $N = 100$, and $M = 2116$; (c) $m = 1.582$, $N = 100$, and $M = 3433$; (d) $m = 2.3$, $N = 100$, and $M = 3309$; (e) $m = 3.298$, $N = 100$, and $M = 2815$ and finally (f) $m = 4.75$, $N = 100$, and $M = 2825$. The corresponding averages are: (a) $\bar{\lambda} \simeq -0.995$, (b) $\bar{\lambda} \simeq -0.988$, (c) $\bar{\lambda} \simeq -0.316$, (d) $\bar{\lambda} \simeq -0.217$, (e) $\bar{\lambda} \simeq -0.151$, and (f) $\bar{\lambda} \simeq -0.105$. The dark blue lines are the fits obtained via equation (8) and each one represents the PDF of the respective spectrum. The number of histogram bins is 100.

ORCID iDs

J Odavić ⬤ https://orcid.org/0000-0003-2729-8284
P Mali ⬤ https://orcid.org/0000-0002-3879-5051

References

[1] Mehta M L 2004 *Random Matrices* (Amsterdam: Elsevier)
[2] Wigner E P 1957 *Statistical Properties of Real Symmetric Matrices with Many Dimensions* (Princeton, NJ: Princeton University Press)
[3] Weidenmüller H A and Mitchell G E 2009 *Rev. Mod. Phys.* **81** 539–89
[4] Eynard B, Kimura T and Ribault S 2018 arXiv:1510.04430
[5] Beenakker C W J 1997 *Rev. Mod. Phys.* **69** 731–808
[6] Livan G, Novaes M and Vivo P 2018 *Introduction to Random Matrices: Theory and Practice* (Berlin: Springer)
[7] Bronk B V 1964 *J. Math. Phys.* **5** 215–20
[8] Marčenko V A and Pastur L A 1967 *Math. USSR Sb.* **1** 457–83
[9] Casati G, Izrailev F and Molinari L 1991 *J. Phys. A: Math. Gen.* **24** 4755–62
[10] Gur-Ari G, Hanada M and Shenker S H 2016 *J. High Energy Phys.* JHEP02(2016)091
[11] Hanada M, Shimada H and Tezuka M 2018 *Phys. Rev.* E **97** 022224

[12] Skokos C H, Gottwald G A and Laskar J (eds) 2016 *Chaos Detection and Predictability* (*Lecture Notes in Physics*) (Berlin: Springer)

[13] Patra S K and Ghosh A 2016 *Phys. Rev.* E **93** 032208

[14] Ahlers V, Zillmer R and Pikovsky A 2001 *Phys. Rev.* E **63** 036213

[15] Braun O M and Kivshar Y S 2013 *The Frenkel–Kontorova Model: Concepts, Methods, and Applications* (Berlin: Springer)

[16] Thorne R E, Hubacek J S, Lyons W G, Lyding J W and Tucker J R 1988 *Phys. Rev.* B **37** 10055–67

[17] Sokolović I, Mali P, Odavić J, Radošević S, Medvedeva S Y, Botha A E, Shukrinov Y M and Tekić J 2017 *Phys. Rev.* E **96** 022210

[18] Juniper M P N, Straube A V, Besseling R, Aarts D G A L and Dullens R P A 2015 *Nat. Commun.* **6** 1–7

[19] Pfeiffer J, Abdumalikov A A, Schuster M and Ustinov A V 2008 *Phys. Rev.* B **77** 024511

[20] Wolf A, Swift J B, Swinney H L and Vastano J A 1985 *Physica* D **16** 285

[21] Pikovsky A and Politi A 2016 *Lyapunov Exponents: A Tool to Explore Complex Dynamics* (Cambridge: Cambridge University Press)

[22] Crisanti A, Paladin G and Vulpiani A 1993 *Products of Random Matrices: In Statistical Physics Springer Series in Solid-State Sciences* (Berlin: Springer)

[23] Eckmann J-P and Wayne C E 1988 *J. Stat. Phys.* **50** 853–78

[24] Cuevas-Maraver J, Kevrekidis P and Williams F 2014 *The Sine-Gordon Model and its Applications: From Pendula and Josephson Junctions to Gravity and High-Energy Physics* (*Nonlinear Systems and Complexity*) (Berlin: Springer)

[25] McLaughlin D W and Scott A C 1978 *Phys. Rev.* A **18** 1652–80

[26] Tekić J and Mali P 2015 *The Ac Driven Frenkel–Kontorova Model* (University of Novi Sad) (https://doi.org/10.13140/RG.2.1.2776.2003)

[27] Floría L M and Mazo J J 1996 *Adv. Phys.* **45** 505–98

[28] Vanossi A, Manini N, Urbakh M, Zapperi S and Tosatti E 2013 *Rev. Mod. Phys.* **85** 529–52

[29] Ustinov A V, Cirillo M and Malomed B A 1993 *Phys. Rev.* B **47** 8357–60

[30] Odavić J, Mali P, Tekić J, Pantić M and Pavkov-Hrvojević M 2017 *Commun. Nonlinear Sci. Numer. Simul.* **47** 100–8

[31] Falo F, Floría L M, Martínez P J and Mazo J J 1993 *Phys. Rev.* B **48** 7434–7

[32] Baesens C and MacKay R S 2003 *Nonlinearity* **17** 567–80

[33] Hindmarsh a serial Fortran solvers for ODE initial value problems (https://computing.llnl.gov/casc/odepack/)

[34] Reichhardt C and Olson Reichhardt C J 2016 *Rep. Prog. Phys.* **80** 026501

[35] Tekić J, Botha A E, Mali P and Shukrinov Y M 2019 *Phys. Rev.* E **99** 022206

[36] Rossler O E 1979 *Phys. Lett.* A **71** 155–7

[37] Matsumoto T, Chua L and Kobayashi K 1986 *IEEE Trans. Circuits Syst.* **33** 1143–7

[38] Benettin G, Galgani L, Giorgilli A and Strelcyn J-M 1980 *Meccanica* **15** 21–30

[39] Shimada I and Nagashima T 1979 *Prog. Theor. Phys.* **61** 1605–16

[40] Ramasubramanian K and Sriram M S 2000 *Physica* D **139** 72–86

[41] Prasad A and Ramaswamy R 1999 *Phys. Rev.* E **60** 2761–6

[42] Jalabert R A and Pastawski H M 2001 *Phys. Rev. Lett.* **86** 2490–3

[43] Tarkhov A E, Wimberger S and Fine B V 2017 *Phys. Rev.* A **96** 023624

[44] Veble G and Prosen T 2004 *Phys. Rev. Lett.* **92** 034101

[45] Kautz R L and Monaco R 1985 *J. Appl. Phys.* **57** 875–89

[46] Shukrinov Y M, Azemtsa-Donfack H and Botha A E 2015 *JETP Lett.* **101** 251–7

[47] Dietz B and Haake F 1990 *Z. Phys.* B **80** 153–8

[48] Odavić J, Mali P and Tekić J 2015 *Phys. Rev.* E **91** 052904

[49] Strunz T and Elmer F-J 1998 *Phys. Rev.* E **58** 1612–20

[50] Middleton A A 1992 *Phys. Rev. Lett.* **68** 670–3

[51] Slijepčević S 2015 *Chaos* **25** 083108

[52] Rahmonov I R, Tekić J, Mali P, Irie A and Shukrinov Y M 2020 *Phys. Rev.* B **101** 024512

[53] Rahmonov I R, Tekić J, Mali P, Irie A and Shukrinov Y M 2020 *Phys. Rev.* B **101** 089901 (erratum)

[54] Atas Y Y, Bogomolny E, Giraud O and Roux G 2013 *Phys. Rev. Lett.* **110** 084101

[55] Oganesyan V and Huse D A 2007 *Phys. Rev.* B **75** 155111

[56] Ott E 2002 *Chaos in Dynamical Systems* (Cambridge: Cambridge University Press)

[57] Prasad A and Ramaswamy R 1999 *Phys. Rev.* E **60** 2761–6

[58] Tracy C A and Widom H 1994 *Commun. Math. Phys.* **161** 289–309

[59] Edelman A and Wang Y 2013 *Random Matrix Theory and its Innovative Applications* vol 66 (Berlin: Springer) pp 91–116

[60] Majumdar S N 2007 arXiv:cond-mat/0701193
[61] Tracy C A and Widom H 1994 *Commun. Math. Phys.* **159** 151–74
[62] Baik J, Deift P and Johansson K 1999 *J. Am. Math. Soc.* **12** 1119–78
[63] Takeuchi K A, Sano M, Sasamoto T and Spohn H 2011 *Sci. Rep.* **1** 1–5
[64] Sasamoto T and Spohn H 2010 *Phys. Rev. Lett.* **104** 230602
[65] Majumdar S N and Schehr G 2014 *J. Stat. Mech.* P01012
[66] Zwillinger D and Kokoska S 2000 *Standard Probability and Statistical Tables and Formulae* (London: Chapman and Hall)
[67] Bornemann F 2010 *Markov Process Relat. Fields* **16** 803–66
[68] Poilblanc D, Ziman T, Bellissard J, Mila F and Montambaux G 1993 *Europhys. Lett.* **22** 537–42
[69] Laffargue T, Lam K-D N T, Kurchan J and Tailleur J 2013 *J. Phys. A: Math. Theor.* **46** 254002
[70] Scientific Computing Research Group SCORG https://scorg.pmf.uns.ac.rs/